Provided for non-commercial research and education use.
Not for reproduction, distribution or commercial use.

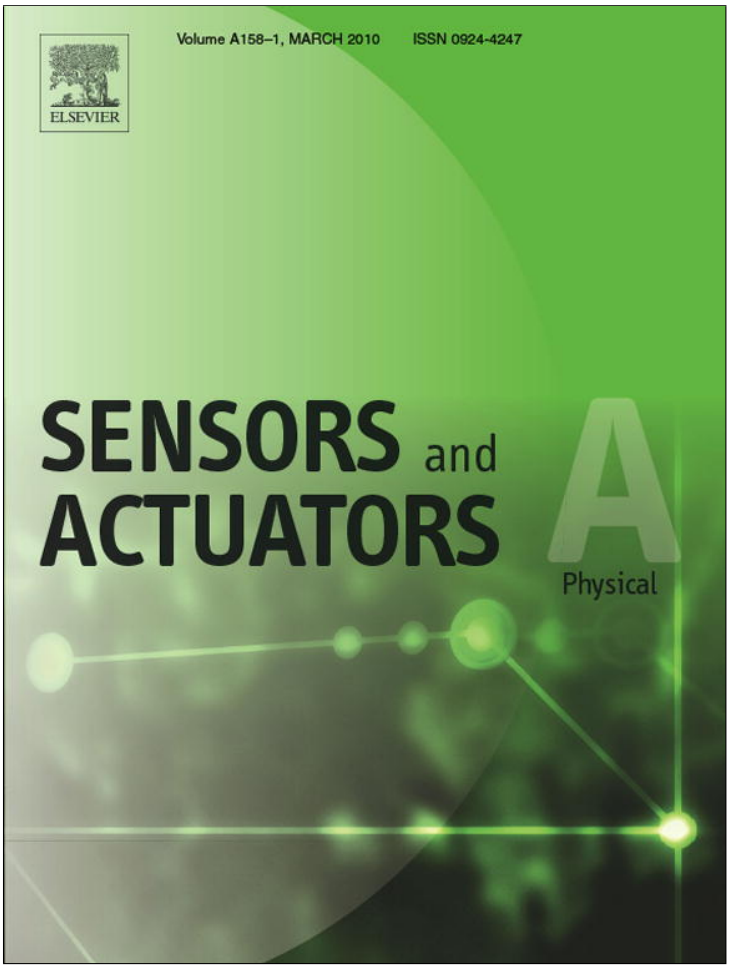

This article appeared in a journal published by Elsevier. The attached copy is furnished to the author for internal non-commercial research and education use, including for instruction at the authors institution and sharing with colleagues.

Other uses, including reproduction and distribution, or selling or licensing copies, or posting to personal, institutional or third party websites are prohibited.

In most cases authors are permitted to post their version of the article (e.g. in Word or Tex form) to their personal website or institutional repository. Authors requiring further information regarding Elsevier's archiving and manuscript policies are encouraged to visit:

http://www.elsevier.com/copyright

Author's personal copy

Sensors and Actuators A 158 (2010) 121–131

Contents lists available at ScienceDirect

Sensors and Actuators A: Physical

journal homepage: www.elsevier.com/locate/sna

A novel diaphragm micropump actuated by conjugated polymer petals: Fabrication, modeling, and experimental results

Yang Fang, Xiaobo Tan*

Smart Microsystems Laboratory, Department of Electrical & Computer Engineering, Michigan State University, East Lansing, MI 48824, USA

ARTICLE INFO

Article history:
Received 4 August 2009
Received in revised form 3 December 2009
Accepted 11 December 2009
Available online 29 December 2009

Keywords:
Conjugated polymer
Polypyrrole (PPy)
Micropump
Modeling

ABSTRACT

Micropumps have promising applications in biomedical devices and micro total analysis systems. Conjugated polymer actuators provide an important potential mechanism for realizing micropumps because of their amenability to miniaturization and low actuation voltages. In this paper we present a novel, conjugated polymer petal-actuated diaphragm micropump, which is in contrast to the typical diaphragm design of using a single piece of soft actuation material clamped at all edges. We show through analysis and experiments that the new design, by alleviating the edge constrains, can provide significantly larger diaphragm deformation and consequently higher flow rate. A physics-based, control-oriented model is developed to predict the diaphragm deformation and the flow rate given the actuation voltage input. Experiments conducted on a polypyrrole (PPy)-actuated micropump, fabricated through PDMS-based MEMS processes, have validated the dynamic model. A maximum flow rate of 1260 μL/min is achieved for the petal-actuated diaphragm pump under an actuation voltage of 4 V, while in comparison, the pump with traditional diaphragm design generates no observable flow under the same voltage.

© 2009 Elsevier B.V. All rights reserved.

1. Introduction

With the advances in microfabrication technologies, micropumps have received extensive attention over the past three decades because of their potential applications in drug delivery, biological and chemical analysis, microelectronics cooling, and space exploration [1]. The actuation mechanisms, fabrication methods, and applications for micropumps have been surveyed in several recent review articles [1–4]. Micropumps can be classified into *displacement pumps*, where the pressure forces are exerted through some moving boundaries, or *dynamic pumps*, where energy is imparted into the working fluid in other means [1]. A related classification is *mechanical pumps* versus *non-mechanical pumps*, depending on whether the pumping mechanism requires moving parts [4].

A predominant class of micropumps operates through periodic displacement of a flexible diaphragm, which changes the volume and thus the pressure of the pumping chamber. Diaphragm movement has been realized through a number of actuation methods, such as electrostatic [5,6], piezoelectric [7–9], thermopneumatic [10–12], shape memory alloy [13,14], electromagnetic [15], liquid–vapor phase change [16], and P(VDF-TrFE)-based electroactive polymer actuation [17]. Pumping can also be achieved by dragging ions in the fluid with electromagnetic fields, examples of which are electrohydrodynamic [18], magnetohydrodynamic [19], and electroosmotic [20] micropumps. Additional reported mechanisms for micropumps include electrowetting [21], bubble expansion and collapse [22], ultrasonic flexural plate waves [23], and evaporation [24]. More information about various micropumps can be found in [1–4] and the references therein.

Ionic electroactive polymers (EAPs), such as conjugated polymers [25–28] and ionic polymer–metal composites (IPMCs) [29–33], have emerged as promising, soft sensing and actuation materials for MEMS devices, robots, and biomedical systems. These materials can produce large deformation under low actuation voltages (several volts), which makes them an attractive actuation choice for diaphragm micropumps. IPMC-actuated micropumps have been studied in simulation [34] and in experiments [35,36] by a few research groups, and a conjugated polymer-actuated diaphragm pump has also been reported [37]. EAP-based micropumps have typically adopted a whole diaphragm design, where a single piece of EAP clamped at all edges acts as the pumping diaphragm [17,35–37]. These edge constraints, however, severely limit the displacement of the diaphragm and thus the pumping performance. Nguyen et al. proposed a flexible support structure for an IPMC diaphragm, which reduced the edge constraints and resulted in higher flow rates [36].

In this paper, we present a novel, conjugated polymer petal-actuated diaphragm micropump, which is in contrast to the typical whole diaphragm design [17,35–37]. We show through modeling analysis that the new design, by alleviating the edge constraints, can provide significantly larger diaphragm deformation

* Corresponding author. Tel.: +1 517 4325671; fax: +1 517 3531980.
E-mail addresses: fangyang@msu.edu (Y. Fang), xbtan@msu.edu, xbtan@egr.msu.edu (X. Tan).

0924-4247/$ – see front matter © 2009 Elsevier B.V. All rights reserved.
doi:10.1016/j.sna.2009.12.012

Author's personal copy

and consequently the higher flow rate. In particular, an analytical model is developed to capture the relationship between the flow rate and the actuation voltage, which includes three parts: an admittance module, an electromechanical coupling module, and a mechanical module. The mechanical module for the cases of both a petal-shape diaphragm and a whole diaphragm is developed using the energy method [38], which incorporates the elastic energy stored in the diaphragm and the work done on the fluid by the diaphragm. The final model for the petal-shape diaphragm pump, after model reduction, is represented as a finite-dimensional transfer function that captures the fundamental physics of conjugated polymer actuators and their interactions with flexible diaphragm and fluid. It will be instrumental in the control design for the pump.

The rest of the pump is fabricated through PDMS-based MEMS processes. Experiments are conducted to evaluate the pump performance and the effectiveness of the model. Both a whole polypyrrole (PPy) diaphragm and a PPy petal-actuated diaphragm are used to test the flow rate in the same pump. While the single PPy diaphragm cannot generate an observable flow, the petal-actuated diaphragm can generate a maximum flow rate of 1260 μL/min and a maximum backpressure of 1.3 kPa under an actuation voltage of 4 V. Furthermore, the measured admittance, deformation curvature, and flow rate are found to match the models well. The complete model predicts that there is an optimal operating frequency for generating the largest flow rate, which is also verified in experiments. The power efficiency of the presented micropump, in terms of power consumed per flow rate, is about four times of that for the PPy-actuated whole diaphragm pump reported in [37].

The remainder of the paper is organized as follows. The design and fabrication of the micropump are described in Section 2. Model development is carried out in Section 3. Experimental results on pump performance and model validation are presented in Section 4. Finally, future work and concluding remarks are provided in Section 5.

2. Design and fabrication of micropump

2.1. Diaphragm designs

In a typical design of EAP-based pumping diaphragm, one uses a single EAP plate as the diaphragm to seal the pump chamber directly. The edge of the plate is mechanically fixed with electrodes on both sides. However, the strain of the middle-plane will be nonzero due to the restriction at the edge, which implies that a significant portion of energy will be required to stretch the middle-plane. The latter constrains the displacement of the diaphragm in the vertical direction. Detailed analysis will be shown in Section 3.

A new design is thus proposed here for the generation of large out-of-plane deformation, as illustrated in Fig. 1. A passive membrane with low stiffness is used to seal the chamber. Then a conjugated polymer plate is cut into the shape of petals and bonded to this passive layer. When the voltage is applied, the conjugated polymer petals will bend together to move the elastic diaphragm

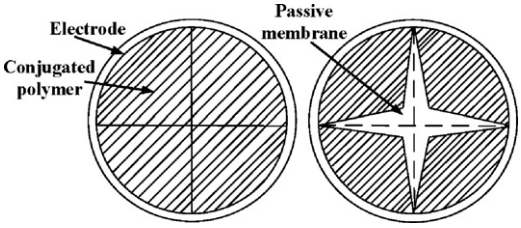

Fig. 1. Schematic representation of a petal-shape pumping diaphragm (top view). Left: before actuation; right: upon actuation.

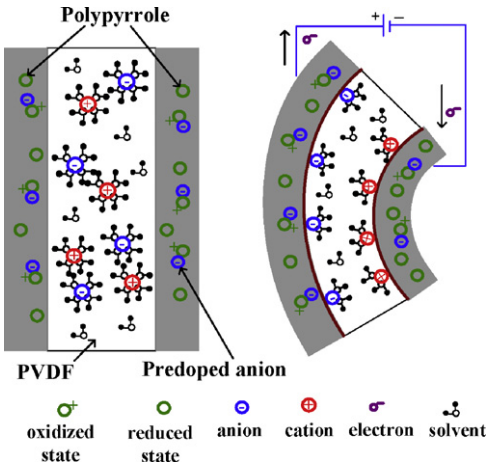

Fig. 2. Illustration of the actuation mechanism of a trilayer polypyrrole actuator. Left: the sectional view of the trilayer structure; right: bending upon application of a voltage.

and generate pressure changes inside the chamber. Therefore, it is the passive layer instead of the conjugated polymer that is being stretched, and one can choose a passive layer material with low Young's modulus to significantly reduce the energy required to stretch the middle-plane.

2.2. Fabrication and assembly of micropump

2.2.1. Fabrication of PPy actuator

In this paper we use a trilayer-structured PPy actuator as the pumping mechanism. The trilayer PPy actuator is illustrated in Fig. 2. On both sides of the actuator are the PPy layers (30 μm each) doped with anions $TFSi^-$, which were electrochemically deposited on the polyvinylidene fluoride (PVDF) layer (110 μm thick). The PVDF layer is amorphous and porous, which serves both as a substrate and a storage tank for the electrolyte. The electrolyte used in this paper is 0.1 M lithium triflouromethanesulfonimide (Li^+TFSI^-) in the solvent propylene carbonate (PC).

When a voltage is applied across the actuator, the PPy layer on the anode side is oxidized while that on the cathode side is reduced. The reduction–oxidation (redox) process can be described as

$$\begin{aligned} \text{Oxidation}: &\quad PPy + TFSI^- \rightarrow PPy^+TFSI^- + e^- \\ \text{Reduction}: &\quad PPy^+TFSI^- + e^- \rightarrow PPy + TFSI^-, \end{aligned}$$

where PPy represents the neutral state of polypyrrole, PPy^+ denotes the oxidized state, PPy^+TFSI^- indicates that $TFSI^-$ is incorporated into the polymer, and e^- denotes an electron. The different volume changes in the two PPy layers lead to bending of the actuator, as shown in Fig. 2(right).

Fabrication of trilayer conjugated polymer actuators is achieved by electrochemically oxidizing pyrrole monomer from a solution to grow PPy layers on either side of a gold-coated porous PVDF film, which acts as the working electrode. The porous PVDF films, obtained from Sigma–Aldrich, has a thickness of 110 μm with pore size of 0.45 μm. It is coated with a thin layer of gold (approximately 100 nm) via sputtering. This ensures a good conductivity therefore good electrochemical growth of PPy. The electrolyte is a solution of 0.1 M pyrrole, 0.1 M Li^+TFSI^- in propylene carbonate (PC) with 0.5 w/w% water. Note that the solution with Li^+TFSI^- will dope the PPy with $TFSI^-$. This fabrication approach follows that in [39,40]. The dopant can be changed to other ions, such as PF_6^-, by changing Li^+TFSI^- to the salts containing those ions.

A potentiostat (Omni 101B, ESA Biosciences Inc.) is used in the electrochemical deposition, which keeps the potential of the

Author's personal copy

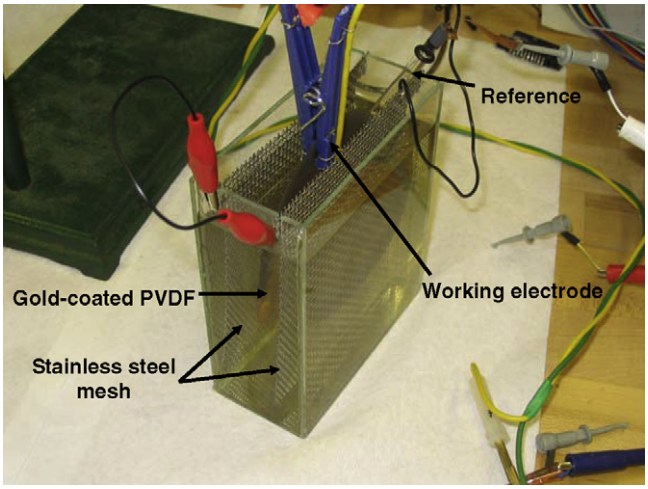

Fig. 3. The setup for fabricating trilayer conjugated polymer.

working electrode at a constant level with respect to the reference electrode in the electrolyte. The cell is a cubic glass container. Two stainless steel meshes are used as the counter electrode, and the PVDF membrane is sandwiched between them to ensure even PPy deposition. A part of the film is left protruding out of the electrolyte for electrical connection. The deposition setup is shown in Fig. 3, and one piece of fabricated trilayer conjugated polymer is shown in Fig. 4.

2.2.2. Fabrication of the rest of the pump

Polydimethylsiloxane (PDMS) is chosen as the material for fabricating the micropump. It is an elastomeric polymer that is much more compliant than silicon or glass, and it is becoming popular for microfluidic devices. The Young's modulus of PDMS varies between 360 and 870 kPa [41]. Other attractive features of PDMS include biocompatibility, low cost, and transparent view (which makes it easy to monitor the fluid flow). The PDMS material is composed of two parts, a curing agent and the polymer. They are mixed by a certain volume ratio and allowed to cure under a certain temperature. Therefore once the micropatterns are fabricated, the inverse patterns of PDMS can be obtained by applying PDMS on the substrate and peeling it off after it is cured. SU-8 2150 photoresist is exposed with conventional UV (350–400 nm) radiation to make micropatterns on a silicon substrate.

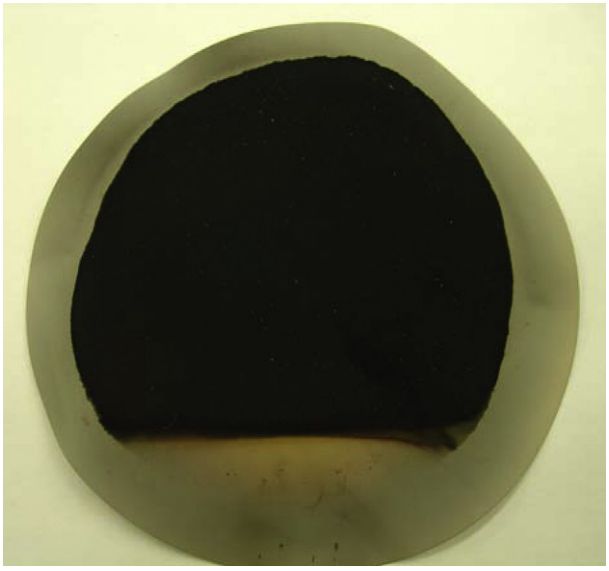

Fig. 4. Fabricated trilayer conjugated polymer.

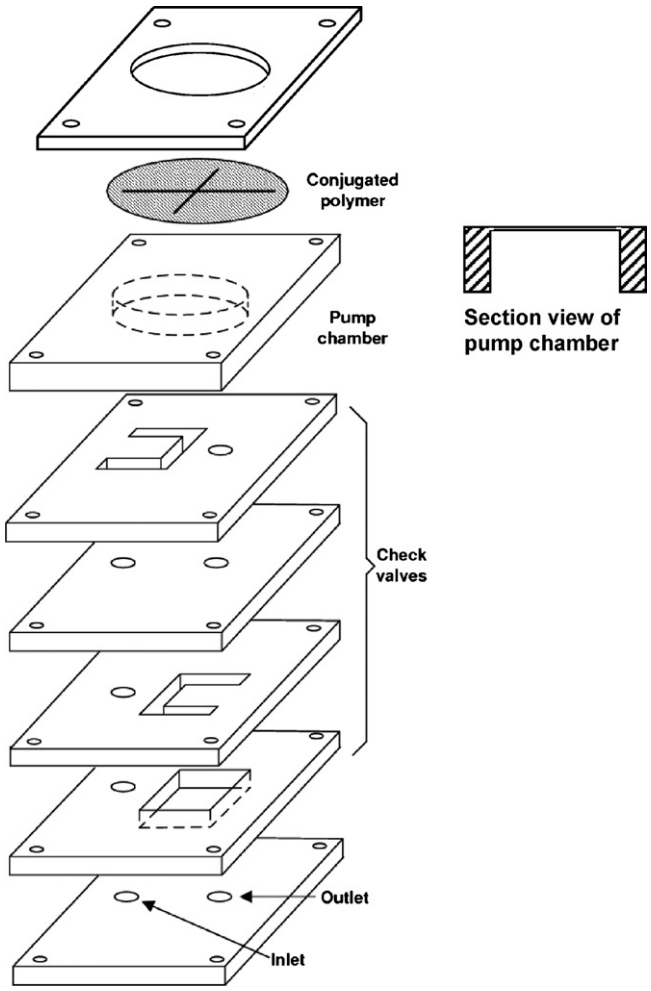

Fig. 5. The assembly schematic of micropump.

By utilizing the microfabrication method involving PDMS and SU-8, different functional layers of the pump can be fabricated and eventually assembled together. The assembly schematic is shown in Fig. 5. Notice that there are four alignment holes at the corners of PDMS layers for the ease of final assembly. The conjugated polymer actuator will be positioned at the top of the pump chamber and attached to the PDMS membrane by applying uncured PDMS as glue.

Flap valves are chosen to keep the directional flow because of their ease of fabrication and high efficiency in regulating the fluid flow. The mechanism of a flap valve is illustrated in Fig. 6. The end of each flap is attached to the middle layer, which has two channels covered by the flaps. When a pressure is applied from the top, the flap on the right will be pushed down and allow the fluid to flow downwards. When a pressure is applied from the bottom, the flap on the left will be lifted up, and the fluid will flow upwards.

The microfabrication process to make the flap valve layer is shown in Fig. 7. Firstly an SU-8 layer is spun on the silicon substrate. Then a photo mask is used to pattern the SU-8 through photolithography. After SU-8 is developed and forms the desired pattern, PDMS is spun on the SU-8 pattern and baked in oven to cure. Finally the PDMS layer is peeled off from the substrate for assembly. Other functional layers can be fabricated in the same way.

The assembled micropump is shown in Fig. 8. The overall size of the pump is 25 mm × 25 mm (top view) and 10 mm (height).

Author's personal copy

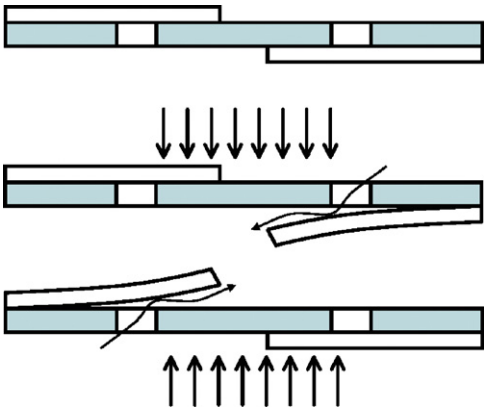

Fig. 6. The mechanism of flap check valves.

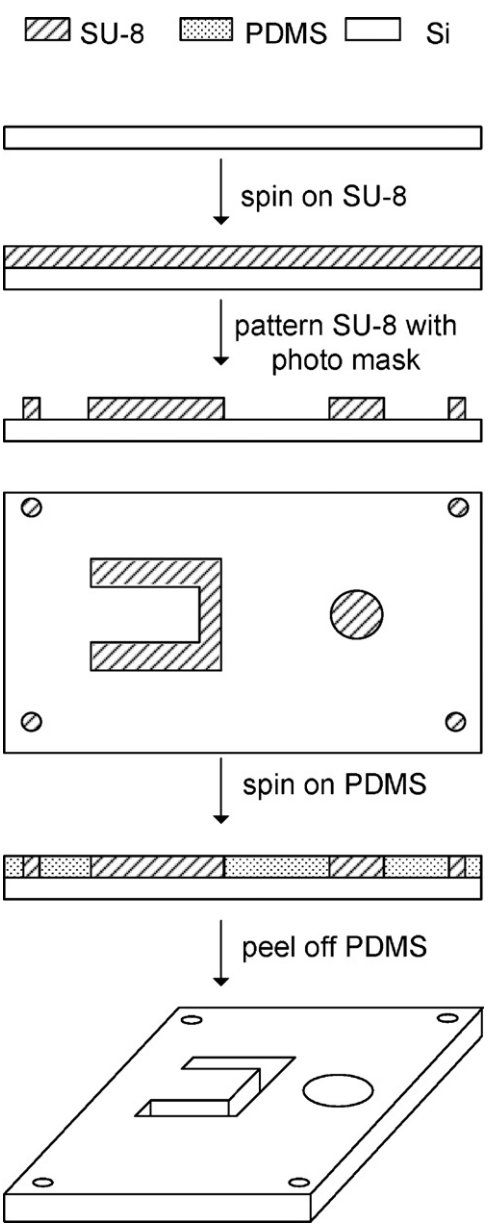

Fig. 7. The microfabrication process to make a flap valve.

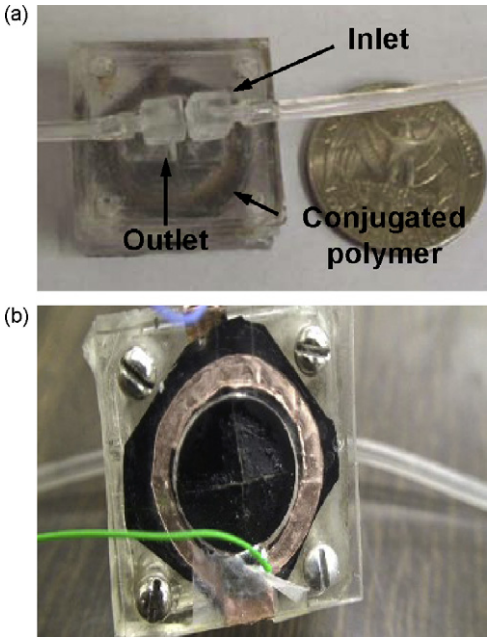

Fig. 8. (a) Top view of the assembled micropump. Two annular copper tapes serve as contact electrodes and are placed in front and back of the conjugated polymer membrane. The conjugated polymer layer appears fuzzy in the picture because of the multiple PDMS layers on top of it; (b) bottom view of the assembled micropump.

Fig. 9. The complete model structure for conjugated polymer actuators.

The diameter of the PPy membrane is 19 mm; excluding the area sandwiched between the plates, the diameter of the free-moving diaphragm is 12 mm. The microchannels have the diameters of 1 mm. The check valve flappers are 1 mm thick, 3 mm wide, and 5 mm long.

3. Physics-based, control-oriented model for the pump

Because PPy has sophisticated electrochemomechanical dynamics that can vary significantly over time [27], a model that captures the complicated dynamics yet amenable to control design is important for applying advanced control algorithms to deliver accurate and consistent flow rates for different applications. As shown in Fig. 9, the developed model in this paper consists of three cascaded modules: (1) the electrical admittance module of PPy relating the current I (and thus the charge transferred) to the voltage input U; (2) the electromechanical coupling module of PPy expressing the generated strain ε_m in terms of the transferred charge; and (3) the mechanical module connecting the generated strain to the diaphragm curvature κ or flow rate Φ of the pump, which captures the dynamics of both the PPy membranes and the flap valves. In this paper, the modules (1) and (2) follow those in [27] and therefore will only be briefly reviewed. Module (3) is derived based on an energy-based method, which will be elaborated in detail.

3.1. Electrical admittance module of PPy

A diffusive-elastic-metal model was proposed for PPy, where it was assumed that the polymer matrix is perfectly conducting and the ion transport within the polymer is solely determined by diffusion [26]. It was adapted to model the ionic dynamics in the

Author's personal copy

trilayer beam [27]. The admittance model of a trilayer conjugated polymer was derived as [27]:

$$\frac{I(s)}{U(s)} = \frac{s[\frac{\sqrt{D}}{\delta}\tanh(h\sqrt{s/D}) + \sqrt{s}]}{\frac{\sqrt{s}}{C} + Rs^{3/2} + R\frac{\sqrt{D}}{\delta}s\tanh(h\sqrt{s/D})}, \quad (1)$$

where $U(s)$ and $I(s)$ are the applied voltage and the resulting current in the Laplace domain, respectively, s is the Laplace variable, δ is the double-layer thickness, D is the diffusion coefficient, R is the resistance across the trilayer polymer, C is the double-layer capacitance, and h is the thickness of the PPy layer. This infinite-dimensional system can be reduced to the following second-order transfer function

$$\frac{I(s)}{U(s)} \approx \frac{Ks(s+z_1)}{(s+p_1)(s+p_2)}, \quad (2)$$

where the parameters are functions of physical parameters [27], which are either known or measurable.

3.2. Electromechanical coupling of PPy

The anions transferred to the polymer cause expansion of the polymer. It can be shown that the strain ε_m introduced by the volumetric change is proportional to the density ρ of the transferred charges [26]:

$$\varepsilon_m = \alpha\rho, \quad (3)$$

where α is the strain-to-charge ratio, which varies for different anions. PPy doped with $TFSI^-$ is used in this paper, and the strain-to-charge ratio is estimated to be $7 \times 10^{-10}\ m^3\ C^{-1}$.

Because the double-layer capacitance is much smaller than the bulk capacitance of the PPy polymer, the charges stored in the double layer at the steady state is negligible comparing with those in the bulk. Therefore one can obtain the density $\rho(s)$:

$$\rho(s) = \frac{I(s)}{s \cdot A \cdot h}, \quad (4)$$

where A is the area of PPy.

3.3. Mechanical module of the micropump

Given the actuation strain ε_m in the PPy layers, an energy-based method is used to model the deformation of the pump diaphragm and consequently the flow rate. In this method the equilibrium of a mechanical structure is obtained by minimizing a properly defined total energy, and such an approach has been taken to predict the curvature of a composite plate generated by the strain mismatch in different layers [38,42,43].

In the following, we first discuss the common framework that applies to both a clamped whole diaphragm and a petal-shape PPy-actuated diaphragm (simply called *petal-shaped diaphragm* hereafter), and then specialize the discussion to individual cases. There are two relevant energy terms: the stored elastic energy and the work done to the fluid.

3.3.1. Elastic energy

In the following analysis, the elastic energy of actuation diaphragm will be calculated based on mechanics of constitutive modeling. The analysis holds for both the whole diaphragm and the petal-shaped diaphragm cases, because the infinitesimal elements in both cases experience radial and transverse strains as defined in Fig. 10. The diaphragm bends as a result of the deformation of all these elements. The difference between the two cases is that the midplane strain ε_0 is fully determined by the diaphragm curvature κ (or vice versa) in the whole diaphragm case because of the edge constraints, while in the petal-shaped diaphragm case, the curvature and the midplane strain are independent from each other.

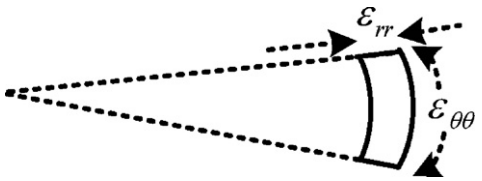

Fig. 10. Definition of the principal strains (view from the top of the diaphragm).

For small deflection, the principal strains defined in Fig. 10 can be expressed as follows [38]:

$$\varepsilon_{rr} = \frac{du}{dr} - z\frac{d^2w}{dr^2} + \varepsilon_s, \quad (5)$$

$$\varepsilon_{\theta\theta} = \frac{u}{r} - \frac{z}{r}\frac{dw}{dr} + \varepsilon_s, \quad (6)$$

where z is the axis in the thickness direction, ε_s is the swelling strain in different layers (ε_m in the oxidized PPy layer, $-\varepsilon_m$ in the reduced PPy layer, and 0 in the PVDF layer), $u(r)$ and $w(r)$ are the radial and transverse displacements of points in the midplane. Note that for the case of a petal-shaped diaphragm, there is a very thin PDMS layer underneath the conjugated polymer to seal the chamber, but the Young's modulus of PDMS used in this paper is 0.5 MPa, which is much smaller than the Young's moduli of PPy (60 MPa) and PVDF (612 MPa) [44]. Therefore, the influence of the PDMS layer on the conjugated polymer deformation is ignored, and the midplane of the PVDF layer is simply taken as that of the PPy-diaphragm structure.

The displacements $u(r)$ and $w(r)$ in the midplane can be expressed as

$$u = \varepsilon_0 r, \quad (7)$$

$$w = \frac{\kappa r^2}{2}, \quad (8)$$

where ε_0 represents the strain of the midplane, and κ is the curvature of the plane as shown in Fig. 11.

Substituting (7) and (8) into (5) and (6), one obtains the following expression

$$\varepsilon_{rr} = \varepsilon_{\theta\theta} = \varepsilon_0 - z \cdot \kappa + \varepsilon_s. \quad (9)$$

The corresponding strain energy density is:

$$\Psi(r,z) = \frac{E_i}{2(1-\nu_i^2)}(\varepsilon_{rr}^2 + \varepsilon_{\theta\theta}^2 + 2\nu_i\varepsilon_{rr}\varepsilon_{\theta\theta}) = \frac{(1+\nu_i)E_i}{1-\nu_i^2}(\varepsilon_0 + \varepsilon_s - z\cdot\kappa)^2, \quad (10)$$

where E_i and ν_i are the Young's modulus and Poisson ratio of the material in the ith layer, which are denoted as E_{PPy} and ν_{PPy} for the PPy layers, and E_{PVDF} and ν_{PVDF} for the PVDF layer. Finally, the

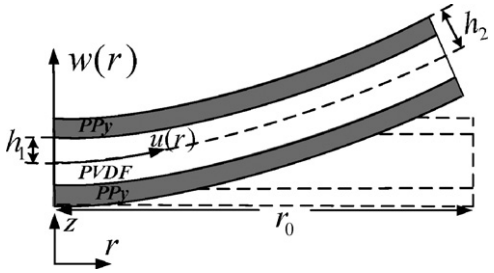

Fig. 11. The coordinates and geometry definition.

Author's personal copy

total strain energy of the trilayer conjugated polymer is obtained by superimposing three energy densities from all layers and integrating over the volume:

$$W_{\text{elastic}} = \int_{-\pi}^{\pi}\int_{0}^{r_0}\left[\int_{-h_2}^{-h_1}\frac{(1+\nu_{PPy})E_{PPy}}{1-\nu_{PPy}^2}(\varepsilon_0-\varepsilon_m-z\cdot\kappa)^2\mathrm{d}z + \int_{-h_1}^{h_1}\frac{(1+\nu_{PVDF})E_{PVDF}}{1-\nu_{PVDF}^2}(\varepsilon_0-z\cdot\kappa)^2\mathrm{d}z + \int_{h_1}^{h_2}\frac{(1+\nu_{PPy})E_{PPy}}{1-\nu_{PPy}^2}(\varepsilon_0+\varepsilon_m-z\cdot\kappa)^2\mathrm{d}z\right]r\mathrm{d}r\mathrm{d}\tau, \quad (11)$$

where r_0 is the radius of the undeformed diaphragm. Since the whole diaphragm and the petal-shaped diaphragm have the same radius under undeformed configuration, r_0 is used in both cases.

3.3.2. Work done on fluid

The work done by the deformed diaphragm needs to be considered in the energy-based method. Considering an incompressible fluid, we have the following equation from the mass conservation principle,

$$\rho V = \rho\int_0^t(\Phi_{in}(\tau)-\Phi_{out}(\tau))\,\mathrm{d}\tau, \quad (12)$$

where ρ is the density of the fluid, Φ_{in} and Φ_{out} are the flow rates at the inlet and the outlet, respectively, with the unit of m^3/s. The relationship between the chamber pressure p and the flow rates is modeled as follows:

$$\frac{\mathrm{d}p}{\mathrm{d}t} = \frac{1}{C_c}(\Phi_{in}-\Phi_{out}), \quad (13)$$

where C_c is the chamber capacitance that can be determined experimentally with the unit of m^3/Pa [45]. Combining (12) and (13), one can obtain

$$p = \frac{V}{C_c}, \quad (14)$$

where $p|_{t=0}$ is considered to be 0, since there is no initial net pressure in the chamber. Therefore, one can express the work done by the diaphragm as

$$W_p = 2\pi\int_0^{r_0}\int_0^{w}p(\tau)\,\mathrm{d}\tau r\,\mathrm{d}r = \frac{2\pi}{C_c}\int_0^{r_0}\int_0^{w}V\,\mathrm{d}\tau r\,\mathrm{d}r. \quad (15)$$

3.3.3. Discussion on individual cases

The total energy is $W = W_{\text{elastic}} + W_p$. For a given actuation-induced swelling strain ε_m, the resulting equilibrium configuration can be found by minimizing the total energy W. We now discuss the explicit forms of W and the corresponding solutions for the cases of a whole diaphragm and a petal-shaped diaphragm, respectively.

The general configuration is characterized by the midplane strain ε_0 and the diaphragm curvature κ, where the curvature is assumed to be uniform. For the whole diaphragm case, however, ε_0 is fully determined by κ (or vice versa) because of the edge constraints. As shown in Appendix A, the volume change V can be approximated by

$$V \approx \frac{\pi r_0^4}{6}\kappa. \quad (16)$$

Substituting (8) and (16) into (15), one can obtain the expression of W_p and consequently W. The equilibrium is reached when $(\mathrm{d}W/\mathrm{d}\kappa) = 0$, which can be rearranged as follows:

$$-36C_1^2r_0^2h_2^2 + (1-\kappa^2r_0^2)\left[\frac{\pi r_0^7}{32C_c}\kappa^2 + (C_2-C_1)r_0h_1^3\kappa^2 + C_1r_0h_2^2(h_2\kappa-3\varepsilon_m)\kappa + 3C_1r_0h_1^2\varepsilon_m\kappa - 6C_1r_0h_2\right]^2 = 0, \quad (17)$$

where

$$C_1 = \frac{(1+\nu_{PPy})E_{PPy}}{1-\nu_{PPy}^2}, \qquad C_2 = \frac{(1+\nu_{PVDF})E_{PVDF}}{1-\nu_{PVDF}^2},$$

The curvature κ can be obtained by numerically solving this equation and appropriately choosing the root.

In the petal-shaped diaphragm case, the volume change V and the work W_p can be approximated by

$$V \approx \frac{\pi r_0^4\kappa}{4}, \quad (18)$$

$$W_p \approx \frac{\pi^2 r_0^8\kappa^2}{12C_c}. \quad (19)$$

The derivation of (18) and (19) can be found in Appendix B.

The equilibrium is reached when $(\partial W/\partial\varepsilon_0) = 0$ and $(\partial W/\partial\kappa) = 0$. Since

$$\frac{\partial W}{\partial\varepsilon_0} = 4\pi r_0^2\varepsilon_0[C_1(h_2-h_1)+C_2h_1], \quad (20)$$

$$\frac{\partial W}{\partial\kappa} = -4\pi r_0^2\left[C_1\varepsilon_m(h_2^2-h_1^2) - \frac{C_1\kappa(h_2^3-h_1^3)}{3} - \frac{C_2\kappa h_1^3}{3}\right] + \frac{\pi^2 r_0^8\kappa}{6C_c}, \quad (21)$$

the equilibrium is:

$$\varepsilon_0 = 0, \quad (22)$$

$$\kappa = \frac{3C_1\varepsilon_m(h_2^2-h_1^2)}{C_1h_2^3 - C_1h_1^3 + C_2h_1^3 + \frac{\pi r_0^6}{8C_c}}. \quad (23)$$

Eq. (23) captures the static deformation of the diaphragm in terms of ε_m. The material damping effect is introduced to incorporate the dynamics during the deformation process. A standard linear solid model [46] is considered. The equivalent modulus E' is represented by

$$E'(s) = E\frac{\alpha'\beta'+\beta'}{\beta'}\cdot\frac{s+\frac{1}{\alpha'\beta'+\beta'}}{s+\frac{1}{\beta'}}, \quad (24)$$

where E is the Young's modulus measured under static condition. The parameters in (24) are chosen to be similar to the values in [47] but with fine tuning to fit the experimental data: $\alpha' = 6.5$ and $\beta' = 0.33$ for PPy, and $\alpha' = 1.88$ and $\beta' = 0.043$ for PVDF. Other damping effects in the pump, such as the flap valve damping, are captured by using the equivalent chamber capacitance that includes a damping term:

$$C_{c'}(s) = \frac{C_c}{1+C_cR_cs}, \quad (25)$$

where R_c represents the equivalent damping resistance with the unit of $\mathrm{Pa\,s/m^3}$.

Thus one can write (23) in the Laplace domain as

$$\kappa = H(s)\cdot\varepsilon_m, \quad (26)$$

where

$$H(s) = \frac{3C_1(h_2^2-h_1^2)}{C_1h_2^3 - C_1h_1^3 + C_2h_1^3 + \frac{3\pi r_0^5}{8C_{c'}}},$$

and C_1, C_2, and $C_{c'}$ are the frequency-dependent terms, because the Young's moduli in (23) are replaced by the ones in (24).

Author's personal copy

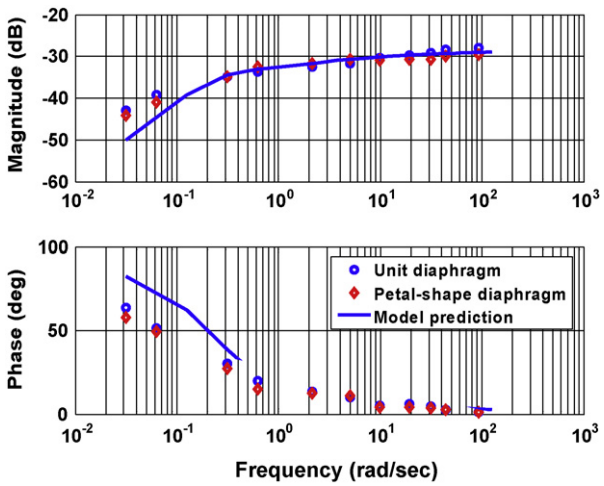

Fig. 12. Comparison of model prediction from (1) with the experimental results for the whole diaphragm and the petal-shaped diaphragm.

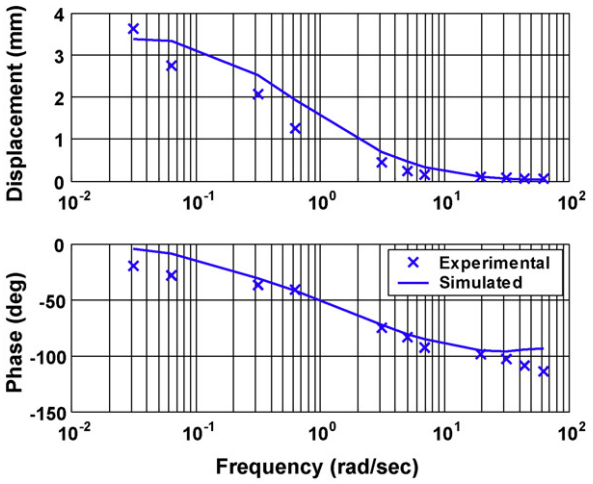

Fig. 13. Comparison of model prediction from (27) with the experimental results for the petal-shaped diaphragm when there is no water (actuation voltage amplitude 4 V).

3.4. Complete model

One can obtain the complete model for the petal-shaped diaphragm in an analytical form by combining (2), (3) and (26), which is shown as follows:

$$\frac{\kappa(s)}{U(s)} = \frac{\alpha K \cdot (s+z_1)H(s)}{A(h_2-h_1)\cdot s(s+p_1)(s+p_2)}. \tag{27}$$

Note that $h = h_2 - h_1$ in (2). However, the complete analytical model for the whole diaphragm is not easy to obtain due to the complexity of (17). Therefore, the model prediction in that case is obtained by numerically solving (17).

Considering (12) and (18), one gets

$$\Phi_{in} - \Phi_{out} = \frac{\pi r_0^4}{4} \cdot s \cdot \kappa. \tag{28}$$

Combining (27) and (28), one can further obtain the transfer function model from the voltage input to the flow rate:

$$\frac{\Phi_{in}(s) - \Phi_{out}(s)}{U(s)} = \frac{\pi r_0^4 \alpha K \cdot (s+z_1)H(s)}{4A(h_2-h_1)\cdot(s+p_1)(s+p_2)}. \tag{29}$$

4. Experimental results

A circular trilayer PPy actuator is used in the experiments. The curvature is measured by a laser sensor (OADM 20I6441/S14F, Baumer Electric Inc.) with a resolution of 5 μm. The model parameter R is identified by applying a relatively high-frequency (100 Hz) sinusoidal input $U\sin(\omega t)$. From (1), the impedance approaches R as $\omega \to \infty$. To measure the parameter C, a step voltage is applied and the transferred charge into the PPy layer is computed by integrating the charging current. The calculation details can be found in [27]. Finally, the resistance and capacitance are identified to be: $R = 27\,\Omega$, $C = 8.69 \times 10^{-5}$ F. The diffusion coefficient D is chosen to be 2×10^{-10} m^2/s based on [26]. The double-layer thickness δ is estimated to be 25 nm based on [47].

4.1. Admittance

Since cutting does not influence the electrical property of conjugated polymer, (1) is used to predict the admittance of both the whole diaphragm and the petal-shape diaphragm. The comparison is shown in Fig. 12, where a good match of admittance is seen between the model and the experimental results.

4.2. Displacement

In experiments the displacement at the center of the diaphragm is measured by a laser distance sensor. The predicted curvature of the petal-shape diaphragm from (27) is used to calculate the displacement based on the following equation [27]:

$$y = \frac{\kappa l^2}{2}, \tag{30}$$

where l is the distance between the clamped end and the laser incident point when the beam is at rest, which is r_0 minus 1 mm in the setup.

The predicted displacements for the petal-shaped diaphragm are compared with the experimental results when there is no water in the pump (Fig. 13) and when pumping water (Fig. 14). There the actuation voltage applied is sinusoidal with an amplitude of 4 V and with different frequencies. All the other parameters in (27) are given or identified in the previous admittance model experiments. C_c and R_c can be determined by fitting the experimental data for the petal-shaped diaphragm. They are identified as $C_c = 1.02 \times 10^{-8}$ m^3/Pa and $R_c = 3 \times 10^8$ Pa s/m^3. To predict the

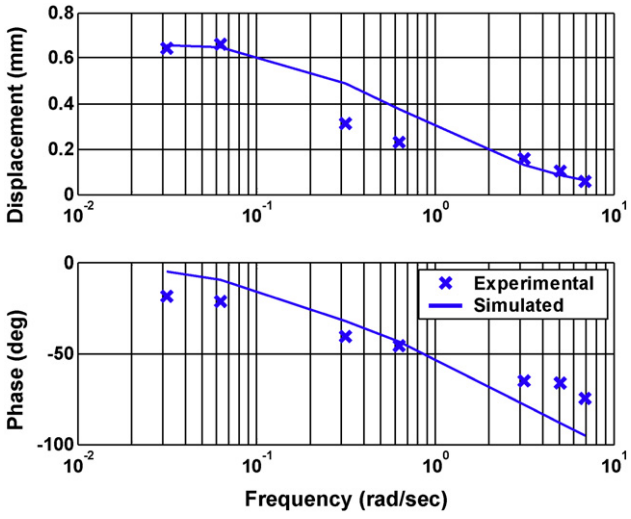

Fig. 14. Comparison of model prediction from (27) with the experimental results for the petal-shaped diaphragm when pumping water (actuation voltage amplitude 4 V).

Author's personal copy

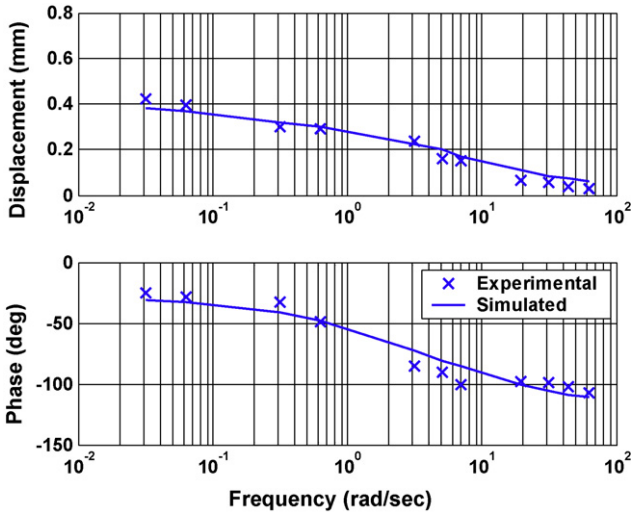

Fig. 15. Comparison of model prediction with the experimental results for the whole diaphragm when there is no water by numerically solving (17) (actuation voltage amplitude 4 V).

results when there is no water in pump, the parameters C_c and R_c are set to be ∞ and 0, respectively, which sets the work done by fluid to be zero.

The experimental results for the whole diaphragm case are also compared with the numerical solution of (2), (3), and (17). The result when there is no water is shown in Fig. 15, while the result when pumping water is shown in Fig. 16. The actuation voltage is 4 V. It can be seen that the petal-shaped diaphragm can generate almost 10 times larger displacement than the whole diaphragm when there is no water in the chamber. When pumping water, the displacement of the petal-shaped diaphragm is almost 3 times larger than the whole diaphragm. These experimental results have proved the effectiveness of the petal-shaped diaphragm design in alleviating the constrains from the clamped edge.

4.3. Flow rate

The backpressure of the petal-shaped diaphragm pump is measured using a setup that is analogous to that in Fig. 7 in [36]. Under an actuation voltage of 4 V, the maximum backpressure achieved is

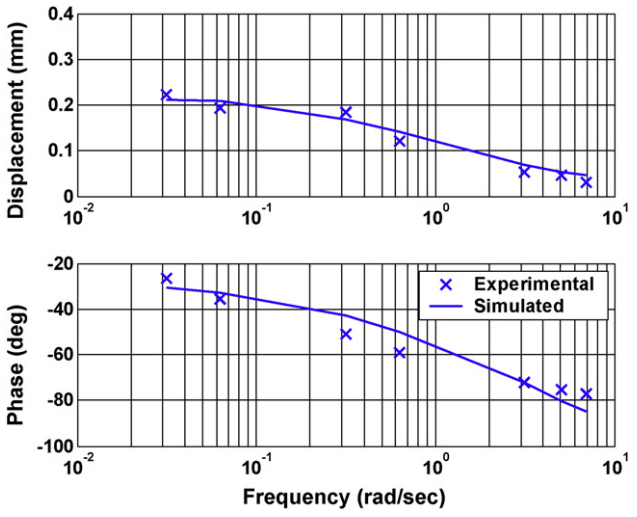

Fig. 16. Comparison of model prediction with the experimental results for the whole diaphragm when pumping water by numerically solving (17) (actuation voltage amplitude 4 V).

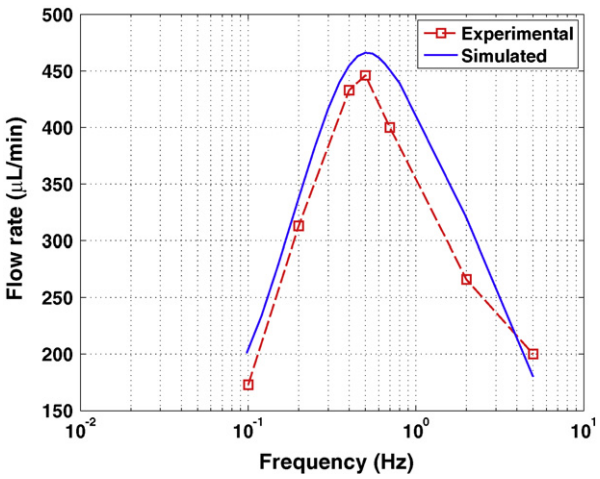

Fig. 17. Flow rate of the petal-shaped diaphragm micropump at different actuation frequencies (voltage amplitude: 2 V).

1.3 kPa. Under zero backpressure, the flow rates are measured and compared with the model prediction (29) for an actuation voltages of 2 V (Fig. 17), 3 V (Fig. 18) and 4 V (Fig. 19). It can be seen that the model can predict the experimental results well under different voltage inputs. The maximum flow rate is 1260 μL/min, which is achieved at about 0.5 Hz. The latter is also predicted well by the model. When the frequency of the input voltage is low, the flow rate is small due to the slow movement of the pump. The flow rate will increase as the operating frequency increases. However, the flow rate will decrease as the frequency becomes higher, because of the damping effect of the flap valves and the declining response of conjugated polymer actuator at high frequencies. Thus the model (29) can facilitate the design optimization and the feedback control of the flow rate. Fig. 20 further shows the measured flow rates versus the applied voltage amplitudes at 0.2 Hz, 0.5 Hz, and 2 Hz. Since voltages of 1 V or lower do not produce enough pressure to push open the check valves and produce an appreciable flow, and it is not advisable to apply a voltage of over 4 V, the figure presents the results under three voltage levels (2, 3, and 4 V). It can be seen that, under each frequency, the flow rate is approximately linear with respect to the applied voltage. On the other hand, the difference between the measurements and a linear approximation indicates the existence of nonlinearities in the system. Such nonlinearities

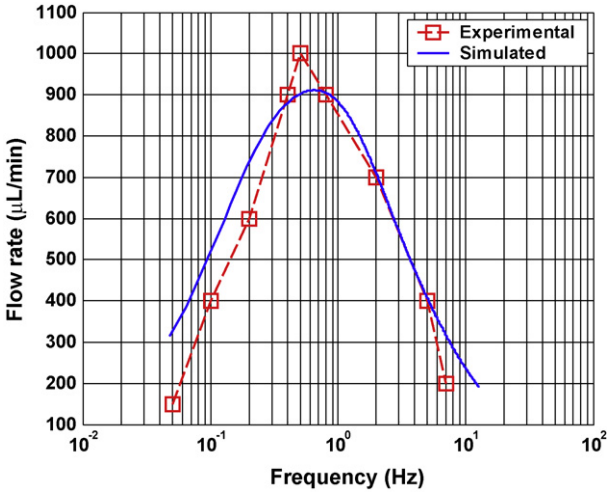

Fig. 18. Flow rate of the petal-shaped diaphragm micropump at different actuation frequencies (voltage amplitude: 3 V).

Author's personal copy

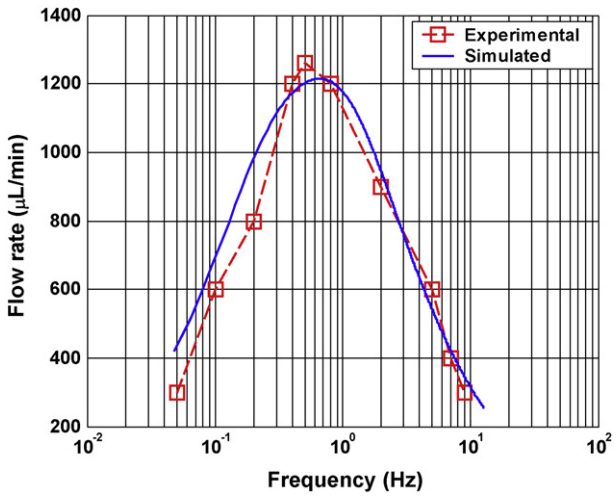

Fig. 19. Flow rate of the petal-shaped diaphragm micropump at different actuation frequencies (voltage amplitude: 4 V).

could arise from both electrochemical dynamics [48] and large mechanical deformation [49], and will be a subject of our future studies.

Fig. 21 shows the electrical power consumed by the pump under an actuation voltage of 4 V, at different frequencies. The power consumption at 0.5 Hz is about 310 mW, with the corresponding flow rate of 1260 μL/min. In comparison, the PPy-based whole diaphragm pump reported by Kim et al. [37] had a flow rate of 52 μL/min with a power consumption of 55 mW. The power efficiency of our pump, in terms of power consumed per μL/min, is thus four times of that in [37]. However, we do realize that the issue of power efficiency involves many factors ranging from materials to test setups, and more care is needed for a fair and thorough comparison between the proposed micropump and others.

We have also tested the pumping performance of the whole diaphragm. However, the flow rate in that case is barely observable, which is most likely because the pressure generated is too low to push open the flap check valves. This has further verified that the clear advantages of the petal-shaped diaphragm design over the traditional whole diaphragm design.

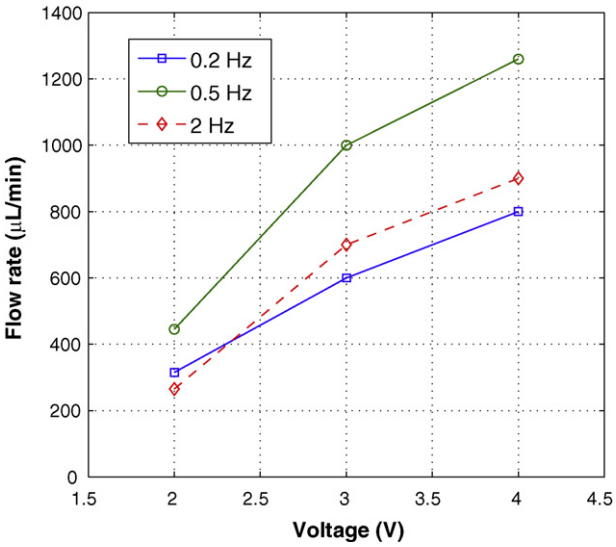

Fig. 20. Measured flow rate versus applied voltage amplitude.

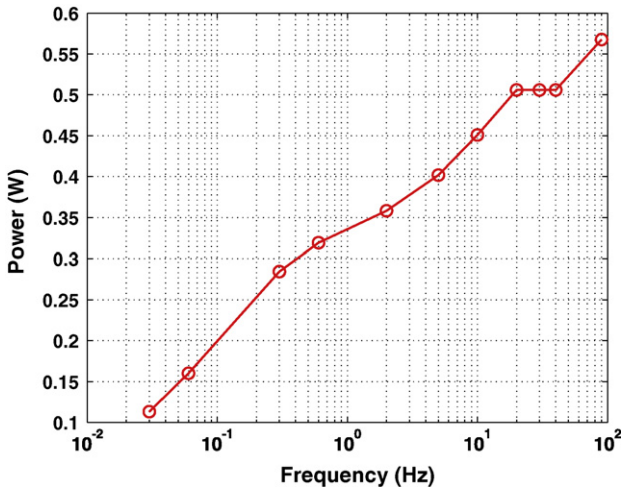

Fig. 21. Electrical power consumed by the pump at different frequencies (voltage amplitude: 4 V).

5. Conclusions and future work

In this paper, circular conjugated polymer actuators are investigated for potential micropump applications. A petal-shaped diaphragm design is proposed to alleviate the constrains from the clamped edge. An analytical model is proposed that captures the relationship between the actuation voltage and the diaphragm deformation/flow rate. Experiments are conducted to verify the model and identify the parameters. The largest flow rate achieved in the current experimental setup is 1260 μL/min, when the operating frequency is about 0.5 Hz. For comparison, modeling analysis and experiments are also conducted on the whole diaphragm case. The model predicted much smaller diaphragm deformation compared with the petal-shaped diaphragm, which is also verified in experiments.

Future work includes refining the pump fabrication process to achieve smaller size and higher pumping efficiency. While existing literature has rarely reported on the efficiency of various micropumps [1], power efficiency is a critical issue when it comes to real applications, and we will calculate and improve the efficiency of the proposed pump by examining the efficiencies in all subsystems. The pump model will also be improved by considering nonlinear effects including nonlinear redox dynamics [48], large deformation of PPy membrane [49], and the dead-zone effect of the check valves. Furthermore, feedback control will be implemented to generate a stable flow rate.

Acknowledgements

This research was supported by an NSF CAREER grant (ECCS 0547131). The authors would like to thank Prof. Gürsel Alici from University of Wollongong for providing very helpful information on the PPy fabrication process, and thank the anonymous reviewers for their useful comments.

Appendix A. Derivation of volume change for the whole diaphragm case

The geometric relationship in a whole diaphragm is illustrated in Fig. 22, where the solid curve represents the sectional view of the midplane of the deformed diaphragm. The midplane strain ε_0 is derived as

$$\varepsilon_0 = \frac{\frac{\theta}{\kappa} - r_0}{r_0} = \frac{\theta}{\kappa r_0} - 1, \tag{31}$$

Author's personal copy

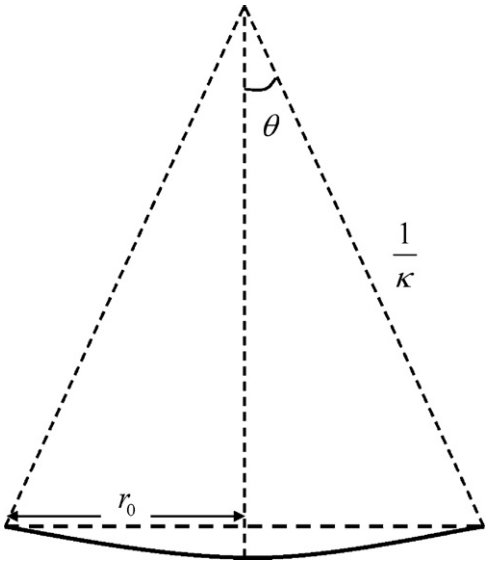

Fig. 22. Illustration of the geometric relationship in the whole diaphragm case.

where $\theta = \arcsin(\kappa r_0)$. From (31), κ can be treated as the only independent variable that characterizes the whole diaphragm configuration.

In the case of the whole diaphragm, the volume change can be characterized by the volume of the dome shown in Fig. 22:

$$V = \frac{\pi}{6} h_0 (3r_0^2 + h_0^2), \tag{32}$$

where h_0 is the height of the dome that equals $R - \sqrt{R^2 - r_0^2}$, and here $R = (1/\kappa)$ denotes the radius of curvature. Substituting this expression into Eq. (32), one has

$$V = \frac{\pi}{3}(R - \sqrt{R^2 - r_0^2})(R^2 + r_0^2 - R\sqrt{R^2 - r_0^2}) \approx \frac{\pi r_0^4}{6}\kappa, \tag{33}$$

where the approximation is based on the Taylor series expansion at $(r_0^2/R^2) = 0$ for $\sqrt{1 - (r_0^2/R^2)}$, since the small deflection of the diaphragm implies that $R \gg r_0$.

Appendix B. Derivation of work W_p for the petal-shaped diaphragm

For the petal-shaped diaphragm, as illustrated in Fig. 23, the following holds when the deflection is small:

$$2\theta \cdot \frac{1}{\kappa} = r_0, \tag{34}$$

which implies

$$\sin\theta \approx \theta = \frac{r_0 \kappa}{2}. \tag{35}$$

The volume change V in the petal-shaped diaphragm case can be approximated by the shadowed volume (a top-off cone) in Fig. 24, under the small deflection assumption. It can be shown that

$$V = \frac{\pi}{2}(r_0^2 + (r_0 - \sin 2\theta \cdot r_0)^2) \cdot 2\sin^2\theta \cdot r_0 \approx \frac{\pi r_0^4 \kappa}{4}. \tag{36}$$

The displacement ξ as defined in Fig. 23 is expressed as

$$\xi = \sin\theta \cdot r_0 \approx \frac{r_0^2 \kappa}{2}. \tag{37}$$

The displacement at each point of the diaphragm, defined as ξ_x in Fig. 23, can be written as

$$\xi_x = \frac{x}{r_0}\xi = \frac{x r_0 \kappa}{2}. \tag{38}$$

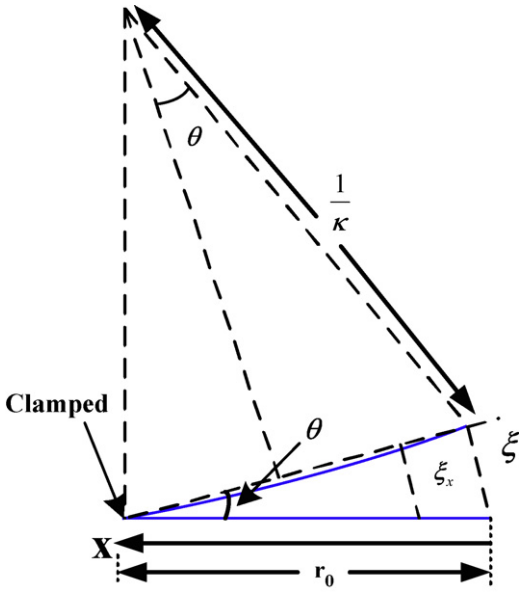

Fig. 23. Illustration of the geometric relationship in the petal-shaped diaphragm case.

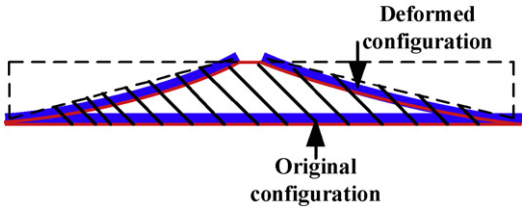

Fig. 24. Approximation of the volume change in the petal-shaped diaphragm case using a top-off cone. The shaded area represents the sectional view of the cone.

By substituting (36) into (15), one can express the work done by the diaphragm as

$$W_p = 2\pi \int_0^{r_0} \int_0^{\xi_x} p(\tau)\, \mathrm{d}\tau r\, \mathrm{d}r = \frac{\pi^2 r_0^8 \kappa^2}{12 C_c}. \tag{39}$$

References

[1] D.J. Laser, J.G. Santiago, A review of micropumps, Journal of Micromechanics and Microengineering 14 (2004) R35–R64.
[2] N.T. Nguyen, X. Huang, T.K. Chuan, MEMS-Micropumps: A review, Journal of Fluids Engineering 124 (2002) 384–392.
[3] P. Woias, Micropumps—past, progress and future prospects, Sensors and Actuators B 105 (2005) 28–38.
[4] A. Nisar, N. Afzulpurkar, B. Mahaisavariya, A. Tuantranont, MEMS-based micropumps in drug delivery and biomedical applications, Sensors and Actuators B 130 (2008) 917–942.
[5] R. Zengerle, J. Ulrich, S. Kluge, M. Richter, A. Richter, A bidirectional silicon micropump, Sensors and Actuators A 50 (1995) 81–86.
[6] A. Machauf, Y. Nemirovsky, U. Dinnar, A membrane micropump electrostatically actuated across the working fluid, Journal of Micromechanics and Microengineering 15 (2005) 2309–2316.
[7] H.T.G. Van Lintel, F.C.M. van De Pol, S. Bouwstra, A piezoelectric micropump based on micromachining of silicon, Sensors and Actuators 15 (2) (1988) 153–167.
[8] M. Koch, N. Harris, A.G.R. Evans, N.M. White, A. Brunnschweiler, A novel micromachined pump based on thick film piezoelectric actuation, Sensors and Actuators A 70 (1998) 98–103.
[9] J.G. Smits, Piezoelectric micropump with three valves working peristaltically, Sensors and Actuators A: Physical 21 (1990) 203–206.
[10] O.C. Jeong, S.S. Yang, Fabrication and test of a thermopneumatic micropump with a corrugated p+diaphragm, Sensors and Actuators A 83 (2000) 249–255.
[11] J.H. Kim, K.H. Na, C.J. Kang, Y.S. Kima, A disposable thermopneumatic actuated micropump stacked with PDMS layers and ITO coated glass, Sensors and Actuators A 120 (2005) 365–369.

Author's personal copy

[12] A. Wego, H.-W. Glock, L. Pagel, S. Richter, Investigations on thermo-pneumatic volume actuators based on PCB technology, Sensors and Actuators A: Physical 93 (2001) 95–102.
[13] D. Xu, L. Wang, G. Ding, Y. Zhou, A. Yu, B. Cai, Characteristics and fabrication of NiTi/Si diaphragm micropump, Sensors and Actuators A 93 (2001) 87–92.
[14] W. Benard, H. Kahn, A. Heuer, Thin-film shape-memory alloy actuated micropumps, Journal of Microelectromechanical Systems 7 (1998) 245–251.
[15] T. Pan, S.J. McDonald, E.M. Kai, B. Ziaie, A magnetically driven PDMS micropump with ball check valves, Journal of Micromechanics and Microengineering 15 (2005) 1021–1026.
[16] W.Y. Sim, H.J. Yoon, O.C. Jeong, S.S. Yang, A phase change type of micropump with aluminum flap valves, Journal of Micromechanics and Microengineering 13 (2003) 286–294.
[17] T.-B. Xu, J. Su, Development, characterization, and theoretical evaluation of electroactive polymer-based micropump diaphragm, Sensors and Actuators A: Physical 121 (2004) 267–274.
[18] J. Darabi, M. Rada, M. Ohadi, J. Lawler, Design, fabrication, and testing of an electrohydrodynamic ion drag micropump, Journal of Microelectromechanical Systems 11 (6) (2002) 684–690.
[19] J. Jang, S.S. Lee, Theoretical and experimental study of MHD (magnetohydrodynamic) micropump, Sensors and Actuators A 80 (1) (2000) 84–89.
[20] T.S. Hansen, K. West, O. Hassager, N.B. Larsen, An all-polymer micropump based on the conductive polymer poly(3,4-ethylenedioxythiophene) and a polyurethane channel system, Journal of Micromechanics and Microengineering 17 (2007) 860–866.
[21] K.S. Yun, I.J. Cho, J.U. Bu, C.J. Kim, E. Yoon, A surface tension driven micropump for low voltage and low power operations, Journal of Microelectromechanical Systems 11 (5) (2002) 454–461.
[22] J.-H. Tsai, L. Lin, A thermal-bubble-actuated micronozzle-diffuser pump, Journal of Microelectromechanical Systems 11 (6) (2002) 661–665.
[23] N.T. Nguyen, A.H. Meng, J. Black, R.M. White, Integrated flow sensor for in situ measurement and control of acoustic streaming in flexural plate wave micropumps, Sensors and Actuators A 79 (2) (2000) 115–121.
[24] C.S. Effenhauser, H. Harttig, P. Kramer, An evaporation-based disposable micropump concept for continuous monitoring applications, Biomedical Microdevices 4 (1) (2002) 27–32.
[25] E. Smela, Conjugated polymer actuators for biomedical applications, Journal of Advanced Materials 15 (6) (2003) 481–494.
[26] J.D.W. Madden, Conducting polymer actuators, PhD thesis, Massachusetts Institute of Technology, 2000.
[27] Y. Fang, X. Tan, G. Alici, Robust adaptive control of conjugated polymer actuators, IEEE Transactions on Control Systems Technology 16 (2008) 600–612.
[28] Y. Wu, D. Zhou, G.M. Spinks, P.C. Innis, W.M. Megill, G.G. Wallace, TITAN: a conducting polymer based microfluidic pump, Smart Materials and Structures 14 (2005) 1511–1516.
[29] Y. Bar-Cohen (Ed.), Electroactive Polymer (EAP) Actuators as Artificial Muscles: Reality, Potential, and Challenges, SPIE–The International Society for Optical Engineering, 2001.
[30] Z. Chen, X. Tan, A dynamic model for ionic polymer-metal composite sensors, Smart Materials and Structures 16 (2007) 1477–1488.
[31] Z. Chen, Y. Shen, N. Xi, X. Tan, Integrated sensing for ionic polymer–metal composite actuators using PVDF thin films, Smart Materials and Structures 16 (2007) S262–S271.
[32] Z. Chen, X. Tan, Monolithic fabrication of ionic polymer–metal composite actuators capable of complex deformation, Sensors and Actuators A, doi:10.1016/j.sna.2009.11.024, in press.
[33] Z. Chen, S. Shatara, X. Tan, Modeling of biomimetic robotic fish propelled by an ionic polymer–metal composite caudal fin, IEEE/ASME Transactions on Mechatronics, doi:10.1109/TMECH.2009.2027812, in press.
[34] S. Lee, K.J. Kim, Design of IPMC actuator-driven valve-less micropump and its flow rate estimation at low Reynolds numbers, Smart Materials and Structures 15 (2006) 1103–1109.
[35] S. Guo, K. Asaka, Polymer-based new type of micropump for bio-medical application, in: Proceedings of the 2003 International Conference on Robotics and Automation, 2003, pp. 1830–1835.
[36] T.T. Nguyen, N.S. Goo, V.K. Nguyen, Y. Yoo, S. Park, Design, fabrication, and experimental characterization of a flap valve IPMC micropump with a flexibly supported diaphragm, Sensors and Actuators A 141 (2008) 640–648.
[37] J.H. Kim, K.T. Lau, R. Shepherd, Y. Wu, G. Wallace, D. Diamond, Performance characteristics of a polypyrrole modified polydimethylsiloxane (PDMS) membrane based microfluidic pump, Sensors and Actuators A: Physical 148 (2008) 239–244.
[38] L.B. Freund, J.A. Floro, E. Chason, Extensions of the Stoney formula for substrate curvature to configurations with thin. substrate or large deformations, Applied Physics Letters 74 (1999) 1987–1989.
[39] G. Alici, P. Metz, G.M. Spinks, A methodology towards geometry optimisation of high performance polypyrrole (PPy) actuators, Smart Materials and Structures 15 (2006) 243–252.
[40] Y. Wu, G. Alici, G.M. Spinks, G.G. Wallace, Fast trilayer polypyrrole bending actuators for high speed applications, Synthetic Metals 156 (2006) 1017–1022.
[41] D. Armani, C. Liu, N. Aluru, Re-configurable fluid circuits by PDMS elastomer micromachining, in: Proceedings of the 12th IEEE International Conference on Micro Electro Mechanical Systems, 1999, pp. 222–227.
[42] S. Huang, X. Zhang, Extension of the Stoney formula for film-substrate systems with gradient stress for MEMS applications, Journal of Micromechanics and Microengineering 16 (2006) 382–389.
[43] V.T. Srikar, S.M. Spearing, A critical review of microscale mechanical testing methods used in the design of microelectromechanical systems, Experimental Mechanics 43 (2003) 238–247.
[44] G. Alici, B. Mui, C. Cook, Bending modeling and its experimental verification for conducting polymer actuators dedicated to manipulation applications, Sensors and Actuators A 126 (2006) 396–404.
[45] R. Bardell, N. Sharma, F. Forster, M. Afromowitz, R. Penney, Designing high-performance micro-pumps based on no-moving-parts valves, Microelectromechanical Systems (MEMS) ASME 62 (1997) 47–53.
[46] I. Ward, Mechanical Properties of Solid Polymers, Wiley, 1979.
[47] Y. Fang, X. Tan, Y. Shen, N. Xi, G. Alici, A scalable model for trilayer conjugated polymer actuators and its experimental validation, Materials Science and Engineering C: Biomimetic and Supramolecular Systems 28 (2008) 421–428.
[48] Y. Fang, X. Tan, G. Alici, Redox level-dependent impedance model for conjugated polymer actuators, Sensors and Actuators B 132 (2008) 182–190.
[49] Y. Fang, T.J. Pence, X. Tan, Nonlinear elastic modeling of differential expansion in trilayer conjugated polymer actuators, Smart Materials and Structures 17 (2008), 065020:1–10.

Biographies

Yang Fang received the Bachelor's degree in Automatic Control and the MS degree in Manufacturing System and Technology from Nanyang Technological University, Singapore, in 2005. He received his PhD degree in electrical engineering at Michigan State University (MSU), East Lansing, in 2009. His PhD dissertation was focused on modeling, control, and applications of conjugated polymer actuators and sensors. He is currently a research engineer with Southwest Research Institute. Dr. Fang was a recipient of the 2008 ASME DSCD Best Mechatronics Paper Award.

Xiaobo Tan received the Bachelor's and Master's degrees in automatic control from Tsinghua University, Beijing, China, in 1995 and 1998, respectively, and the PhD degree in electrical and computer engineering from the University of Maryland, College Park, in 2002.

From September 2002 to July 2004, he was a research associate with the Institute for Systems Research at the University of Maryland. Since August 2004, he has been an assistant professor in the Department of Electrical and Computer Engineering and director of Smart Microsystems Laboratory at Michigan State University. His current research interests include electroactive polymer sensors and actuators, aquatic robotics, modeling and control of smart materials, and adaptive autonomous cyber-physical systems.

Dr. Tan is an associate editor of Automatica and a member of the IEEE Control Systems Society Conference Editorial Board. He was a guest editor of IEEE Control Systems Magazine for its February 2009 issue's special section on modeling and control of hysteresis. He received the NSF CAREER Award in 2006, the 2008 ASME DSCD Best Mechatronics Paper Award, and the Teacher-Scholar Award from Michigan State University in 2010.